Plastic Flow Under Shear-Compression at the Micron Scale-Application on Amorphous Silica at High Strain Rate

Gaylord Guillonneau, Sergio Sao Joao, Benedicte Adogou, Simon Breumier, Guillaume Kermouche

Plastic flow under shear-compression at the micron scale – application on amorphous silica at high strain rate

Gaylord Guillonneau[1*], Sergio Sao Joao[2], Benedicte Adogou[1-2], Simon Breumier[2], Guillaume Kermouche[2]

[1]Université de Lyon, Ecole Centrale de Lyon, LTDS, UMR CNRS 5513, 36 avenue Guy de Collongue, 69134 Ecully, France, 33

[2]Mines Saint-Etienne, CNRS, UMR 5307 LGF, Centre SMS, 42023 Saint Etienne, France, 33

[*]Corresponding author. E-mail: gaylord.guillonneau@ec-lyon.fr

ABSTRACT

A new measurement technique based on microshear was developed. This technique, inspired from a macroscopic test named 'Shear Compression Specimen', was developed at micron scale, by making the specimen using FIB technology, and by compressing it using an in situ SEM nanoindenter. The experimental tests applied on fused silica show a good repeatability of the data, at low and high strain rates ($2000s^{-1}$). Numerical simulation revealed that the deformation in the 'Microshear Compression Specimen' is mainly shear. This approach allows better understanding of surface shear properties at microscale, which is of primary importance for tribological surfaces. It can also help to better understand surface mechanical properties of pressure dependent materials. Finally, since the shear is applied on a very small gauge in the specimen, it opens the way to very high strain-rate experiments (10^4s^{-1} strain rate).

KEYWORDS: shear, high strain rate, micron scale, silica glass, plastic deformation, simulation.

INTRODUCTION

The measurement of mechanical properties at micrometer/nanometer scale is usually performed using instrumented nanoindentation [1], or by recent techniques such as micro-compression, microtension, etc. [2]. They allow the surface properties measurement under different types of loadings like compression or tension, which corresponds to most of materials applications. However, there is still a need to develop micromechanical techniques able to load materials under pure shear. Measuring shearing properties is of primary importance since tribological surfaces are submitted to shear. Unfortunately, classical techniques to measure surface mechanical properties consider only partial shear deformation [3,4]. Also, for amorphous materials like silicate glasses, there is a competition between compression and shear [5,6], at the surface scale. There is thus a need to develop a method permitting to separate the two deformation modes, to get a better understanding of the mechanical behavior of this kind of materials at micrometer scales.

Despite the existence of many techniques to measure shear properties at macroscopic scale, almost no study has focused on the development of this technique at microscale. One can cite Heyer *et al.* who developed a specific geometry on gold single crystal, named 'microdouble shear specimen', first developed by Mayr *et al.* at macroscopic scale [7]. It consists in machining through Focused Ion Beam milling two vertical gauges. This specimen, whose shear gauges dimensions are at the µm order, was compressed by a flat punch, inside a Scanning Electron Microscope. They obtained reliable data despite of the complex geometry to make the specimen. Nevertheless, such a micromechanical test is very sensitive to the misalignment between the tip and the specimen, which can induce a load transfer from one gauge to another [8].

In this paper, a new method to measure surface shear mechanical properties is presented. This technique was inspired from a macroscopic test named "Shear Compression Specimen", first developed by Rittel *et al.* [9–14]. This method consists in compressing a cylindrical pillar, whose two grooves inclined at 45° from the longitudinal direction, are machined at mid-height of the cylinder. The idea is to reproduce the same geometry at micrometer scale, like Ames *et al.* did at an intermediate scale [15,16], using FIB technology, and to compress the "Micro-shear Compression Specimen" (MCS) using a SEM indenter. This type of specimen was chosen because this geometry is relatively easy to machine using a FIB. Also, this specimen implies the shearing of 1 gauge only. The tests were performed on fused silica, as it is the

calibration material used at microscale [1]. Tests were performed at low and high strain rates (until $2000s^{-1}$).

GEOMETRY AND METHOD DESCRIPTION

The MCS geometry is presented on Fig. 1a. The geometry was chosen based on Dorogoy *et al.* specifications [14]. All the MCS were made using a ThermoFisher Helios NanoLab 600i FIB-SEM system. A coarse milling at 30kv and 2.5nA allows to shape the MCS and to clear the area around for visualization. Fine nano-machining at 30kv and 80pA is used to sculpt the groove and complete the preparation. Cylindrical grooves were designed, in order to induce large shear deformation [14]. Three geometries were then tested and are presented in Table I (expected and experimental geometry). The first geometry follows the dimensions prescribed by Dorogoy *et al.* [14]. The second one is used in order to check if a larger groove can change the stress distribution in the gauge, this groove width being also chosen for geometry 3 to avoid cracking at high strain rate. For the third geometry, the ratio H/D was decreased to limit potential bending issues, especially at high strain rate, H and D being the height and the diameter of the MCS. Concerning the experimental dimensions, the difference with the expected value can reach 15-20%. It should be noted that the true experimental geometry of each Microshear Compression Specimen was used to calculate the mechanical properties (equations 1-3).

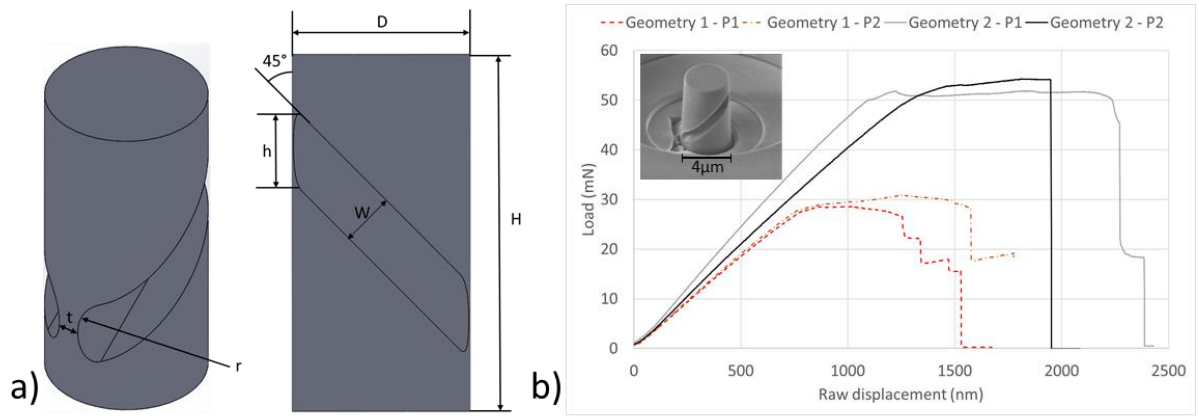

Fig. 1: a) Drawing of the Micro-shear Compression Specimen. b) Load-displacement curves measured using geometries 1 and 2 (inset - Example of geometry 2 machined with FIB).

	Geometry 1		Geometry 2		Geometry 3	
	Expected	Experimental	Expected	Experimental	Expected	Experimental
D (µm)	4.0	4.5	4.0	4.6	4.0	4.4
H (µm)	9.0	9.5	9.0	9.4	6.0	6.3
W (µm)	1.2	1.1	1.2	1.0	1.2	1.0
t (µm)	0.6	0.7	1.2	1.4	1.2	1.5
h (µm)	1.7	1.6	1.7	1.5	1.7	1.4
r (µm)	0.6	0.6	0.6	0.6	0.6	0.6

Table I: Expected and experimental Micro-shear Compression Specimen geometries used in this study. The experimental dimensions correspond to the mean value of several MCS (2 to 6 specimens per geometry). The Dorogoy *et al.* H value must be normally 8µm. The 9µm value was chosen to avoid contact between the gauge lower part and the sample during deformation. The experimental *t* value corresponds to the half value between the width measured on the front face and the one on the rear face. The experimental *D* value corresponds to the half value between the top diameter and the bottom diameter of the pillar. The pillar diameter and the gauge width are not constant because of the conical shape of the ion beam.

Specimens were compressed using an *in situ* SEM nanoindenter from Alemnis [17]. This machine is displacement-controlled, which is of primary importance to measure plastic flow of materials prone to strain-softening such as silicate glasses [18]. A diamond flat punch was used to compress the specimens. This device is equipped of a high dynamic module, enabling high strain rate experiments [19–21]. More specifically, experimental tests were performed at strain rates from 0.04s-1 to 2000s-1. The equivalent strain rate is calculated using the following equation during shear experiments:

$$\dot{\varepsilon}_{eq} = \frac{\dot{d}}{h} \quad (1)$$

$\dot{d}$ being the displacement rate and *h* the gauge height (Fig. 1).

To check the results consistency, micro-compression was also performed on fused silica micropillars. Pillars geometry is detailed in [22]. For micropillar compression, the strain rate is given by $\dot{\varepsilon} = \frac{\dot{d}}{H}$. The strain rate applied on micropillars varies between $0.01s^{-1}$ and $1000s^{-1}$.

In order to extract shear properties, the shear stress and shear strain calculations are necessary. Expressions from Dorogoy *et al.* were used to calculate the plastic equivalent stress $\hat{\sigma}$ and strain $\hat{\varepsilon}_p$ [14]:

$$\hat{\varepsilon}_p = \sum_{i=1}^{N} k_{i+2} \left(\frac{d-d_y}{h}\right)^i \text{ for } d > d_y \quad (2)$$

$$\hat{\sigma} = k_1\left(1 - k_2\hat{\varepsilon}_p\right)\frac{P}{Dt} \text{ for } P > P_y \quad (3)$$

d being the displacement, *dy* and *Py* the displacement and load at yield stress, and *P* the applied load [14]. The *N* value and k_i coefficients are presented in Table II. The experimental MCS dimensions were used in these equations.

The experiments at low strain rate (lower than $0.04s^{-1}$) were performed with the classical nanoindenter, in closed loop mode, whereas higher strain rate experiments were performed in open loop mode, since the speed was too high to regulate correctly the signal.

N	k_1	k_2	k_3	k_4	k_5
3	0.93	0.23	3.40	-3.73	1.8

Table II: Parameters used in the Dorogoy *et al.* expressions.

RESULTS AND DISCUSSION

An example of Micro-shear Compression Specimen is presented on Fig. 1b (inset). This specimen corresponds to geometry 2. As shown here, the grooves design respects well the prescribed geometry. The main issue concerns gauge width. The conical shape of the ion beam – i.e. cone angle about 8° - results in a slightly larger groove section at the bottom of the pillar. The effect of this parameter was checked through a finite element modeling and is detailed in the Supplementary Material. Fig. 1.b displays the load-displacement curves measured on MCS with geometries 1 and 2. A clear threshold is observed permitting to split the deformation into elastic and plastic parts. As observed, the experimental curves are quite repeatable for each geometry, both in the elastic and plastic domains. The load is constant as a function of the displacement in the plastic regime, which is consistent with the absence of strain hardening in silica as reported by Kermouche *et al.* [18]. It is noticed that the elastic parts for geometry 2 samples P1 and P2 are rather different. This is the consequence of the use of a different sample holder for P1 and P2 that affects the device stiffness, the displacement being corrected by the same frame stiffness value on each curve. As the micro-compression test [18], the investigation of the elastic deformation regime with shear-compression test remains therefore quite challenging. In the case of silica, it is possible to identify the device stiffness through post-mortem analysis by fitting the elastic part of the load-displacement curves computed from finite element simulations, since silica elastic domain is rather large. For less elastic materials, the device stiffness has to be measured independently.

In Fig. 2, pictures showing a typical deformation of the MCS are presented (geometry 2) with their corresponding experimental load-displacement curve at low strain rate. On pictures 1 and 2, the MCS is deformed elastically. From pictures 3 to 5, the upper part of the MCS seems to be translated from left to right, whereas the bottom part remains almost not deformed. This movement is consistent with shear strain localization in the gauge. For a larger deformation (not shown here), a global failure of the micro-shear compression specimen happened. A load drop on the load displacement curve is therefore

observed. This failure is likely a consequence of bending torque that is induced by the relative lateral translation of the upper part with respect to the bottom part. Such a torque would lead to high tensile stresses at the extremity of the gauge enabling pillar's brittle failure. It should be figured out that the plane bending can also occur during deformation triggering MCS failure during deformation. This phenomenon can be caused by a misalignment between the flat punch and the pillar top, or the gauge. A future work about misalignment influence on load-displacement curve will be considered in another paper.

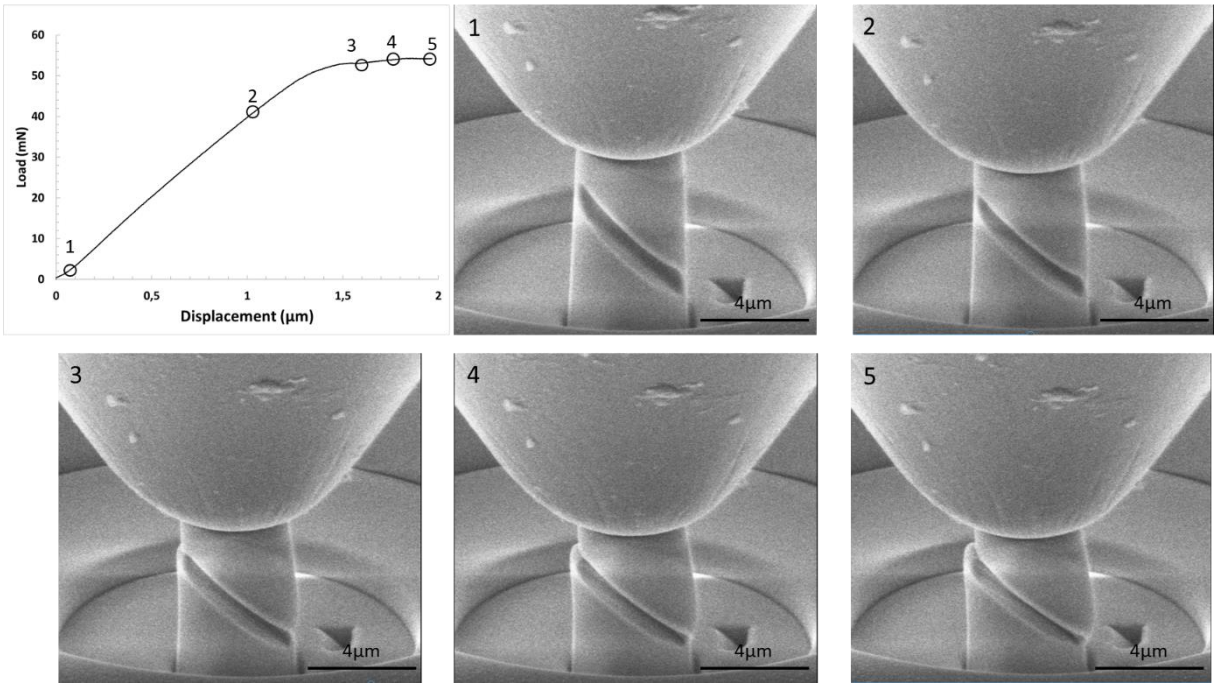

Fig. 2: Load-displacement curve measured by micro-shear and pictures showing the shear deformation of the Micro-shear Compression Specimen at low strain rate (0.04 s^{-1}).

A finite element model was made to check the consistency of experimental results. The exact geometry of the gauge with a larger gauge width at the bottom than at the top (measured on SEM images) was accounted for. Calculations were performed with the Finite Element Software "Abaqus" using Hybrid three dimensional tetrahedral linear elements C3D4H and a finite transformation formulation based on the multiplicative decomposition of the deformation gradient into an elastic and a plastic part and the Jauman objective stress rate. An implicit Finite Element (FE) scheme was used. The flat punch was a rigid body. The compression process was modelled by prescribing a vertical displacement to the flat punch. The friction coefficient acting between the punch and the pillar was assumed at 0.1. Silica was modeled using a simple perfectly plastic J2-shear flow constitutive model as defined in [18]. The yield Stress (von Mises) was 7GPa and the Young modulus was 70GPa (Poisson ratio ~0.2). The densification cannot be accounted for within such a constitutive model. For that extent it would have been necessary to use a porous media-based constitutive model such as the one originally developed to model indentation-induced densification [23]. However, it was shown that densification did not play much a role on the load-displacement curve under pillar compression loading, for which shear flow was demonstrated to be the dominant mechanism. Two finite element analyses were run: one considering that the punch cannot move laterally (fixed punch) and the second one considering that the punch is free to move laterally (free translation). This latter case was closer to the Dorogoy *et al.* macroscopic set up [18], for which a lateral degree of freedom was permitted.

Finite element results related to geometry were plotted on Fig. 3 and compared to the resulting experimental curve. In order to compare experimental and FE-computed load-displacement curves, the device compliance has been identified using the elastic part of the load-displacement curve. In Fig. 3, displacement is thus named 'corrected' displacement to avoid any confusion with the 'raw' displacement of Fig. 1 and 2. It is worth noting the excellent agreement in terms of yield threshold is obtained. Upon

plastic flow, the experimental curve lied in between the FE results, even though it appeared to be closer to the condition of free translation rather than the condition of 'fixed' punch. This means the lateral frame stiffness of the micro shear-compression test is quite low compared to the vertical frame stiffness. For the 'fixed' punch condition, the load was increasing with respect to the displacement whereas the 'free translation' condition led to yielding upon constant load. Similar results were obtained with geometry 1 (smaller gauge). The strain field was localized in the middle of the gauge as expected and appeared as quite homogeneous along the gauge length. It reached a value up to 1.0 and beyond, that is much larger than what could be obtained with micro compression or micro tensile test for which the absence of strain hardening should lead to rapid necking.

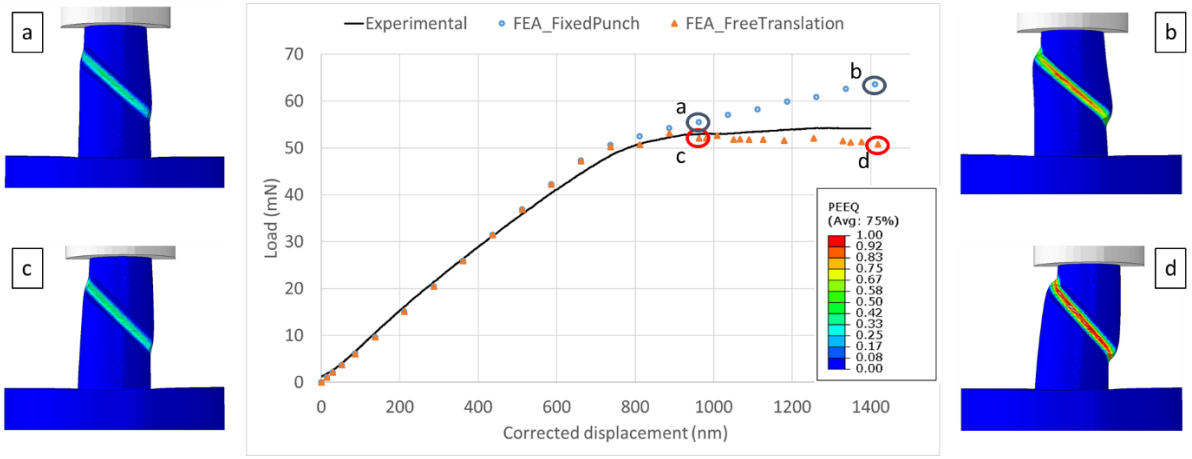

Fig. 3: Comparison between FE results and experimental data for geometry 2. Experimental displacement was corrected by considering device stiffness computed to fit the elastic part of the FE load-displacement curves.

Shear stress-strain curves were derived following the methodology proposed by Dorogoy *et al.* [14] using equations (2) and (3). It should be noted that these equations are valid only in the plastic regime. Consequently, the elastic part was not considered hereafter. Fig. 4 presents the "stress vs plastic strain" curves for different strain rates varying between $0.01s^{-1}$ and $2000s^{-1}$. The yield point (to dissociate elastic and plastic regimes) was determined using the load displacement curve of each sample. The results were compared to those obtained from high strain rate micropillar testing performed on RIE pillars. The corresponding stress-strain curves were derived using the methodology detailed in [18]. The complete true stress-strain curve, including the elastic part, is plotted in the supplementary Fig. S-3. The difference in noise levels on the curves comes from the sampling rate, which is different at low (20Hz sampling rate at 0.01 and 0.04s-1 strain rate) and high strain rates (50kHz). Also, for microshear tests, the combination of several tests could add some dispersion on the data. The shear stress is constant during plastic flow pointing out the absence of shear strain hardening, which was in good agreement with micro-compression tests. Note that the good correlation between micro-compression and microshear data implies a negligible effect of FIB damage on the gauge of MCS, which could be an issue because of the small size of the gauge. Strains up to 0.5 can be measured from shear compression test. For some specimens, strains up to 1.0 were also reported (not shown in Fig. 4) which is consistent with finite element results. Fig. 4 shows that plastic flow of silica is likely not strain-rate dependent up to a strain rate equals $1000s^{-1}$. This is confirmed in Table III where the yield stress measured by micro-compression and shear are presented as a function of the strain rate. Let us note the standard deviation is presented only for shear tests since only one test per strain rate was performed by micro-compression. More especially, the yield stress value calculated for microshear tests was determined on 4 specimens for $0.04s^{-1}$ strain rate experiments, 2 specimens for $500s^{-1}$ strain rate experiments, and 3 specimens for $2000s^{-1}$ strain rate experiments. The shear yield stress seems to slightly increase at higher strain rate (up to $2000s^{-1}$) but should be taken with care because of the sampling frequency limitation (50kHz). This is in accordance with the data of Ramachandramoorty *et al.* who observed a constant yield stress until $1000s^{-1}$, and an increase of the yield stress for higher strain rates, with yield stress values being similar to the present results [24]. However, a strong discrepancy for the low strain rate range is noticed. This

difference was already noticed in a previous paper on micropillars compression [18]. The reason for such a discrepancy is likely related to the pillars geometry used by Ramachandranmoorty *et al.* More specifically, the taper angle of RIE micropillars used in this paper is about 3-4°, which is less than theirs (6°). Also, our RIE micropillars aspect ratio is around 1, which is less than theirs (3.5). Therefore, Ramachandranmoorty *et al.* pillar's geometry would much enhance shear localization and thus shear band nucleation and propagation that are thermally activated phenomena.
It is worth noting the micro-shear compression test designed did not lead to similar strain-rate dependence. It might thus be concluded that the micro-shear compression test is a better tool to investigate homogeneous shear flow than the micropillar compression test.
Regarding amorphous silica, its weak strain-rate dependence and its ability to sustain large shear strain without strain hardening make it as one of the best materials to calibrate nanomechanical testing under high strain rate conditions.

	Microshear		Micro-compression
Strain rate (s-1)	Yield stress (GPa)	Standard deviation (GPa)	Yield stress (GPa)
0.01			6.97
0.04	7.58	0.26	
50			7.32
500	7.56	0.16	7.29
1000			7.86
2000	8.21	0.33	

Table III: Yield stress measured by micro-shear and micro-compression as function of the strain rate.

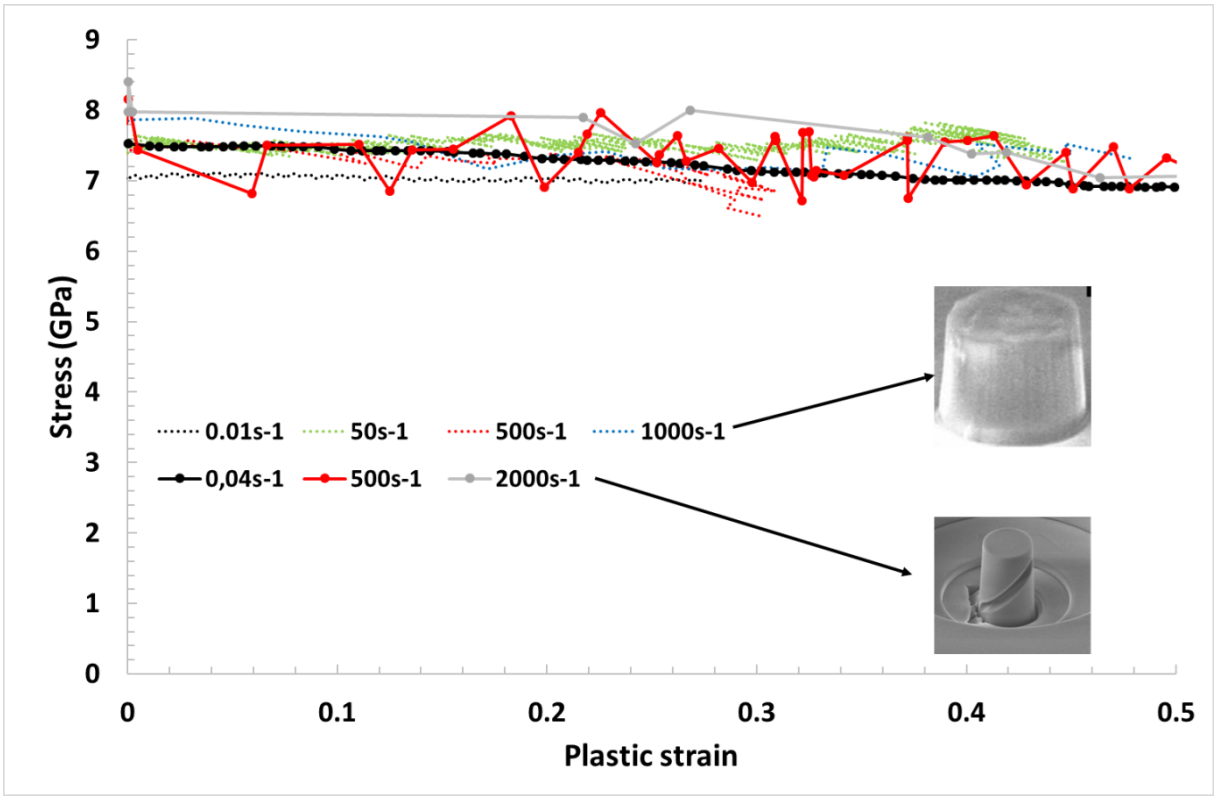

Fig. 4: Shear and compressive stress vs plastic strain as a function of the strain rate for micro-compression and micro-shear compression tests. For shear tests at high strain rate, 2 experiments at $500s^{-1}$ and 3 experiments at $2000s^{-1}$ are plotted together. For shear test at low strain rate ($0.04s^{-1}$) and micro-compression tests, only one curve per strain rate is plotted.

CONCLUSIONS

In this paper, the following conclusions can be drawn:

- A new method to measure shear mechanical properties at microscale, based on MCS, was developed.
- The MCS can be easily machined using FIB technology.
- Experimental data show a good repeatability of the tests, at low and high strain rate, confirming the geometry stability for each specimen.
- Experimental data and numerical simulations revealed that the deformation in the gauge is mainly shear, and the shear strain is uniform along the gauge.
- Plastic flow of amorphous silica can be well captured by a simple J2-shear flow model with no strain hardening.
- No strain rate dependence of amorphous silica yield stress is reported until $1000s^{-1}$, which makes amorphous silica one of the best materials to calibrate nano-mechanical set-ups at very high strain rates.

This new technique opens the way to micro-shear properties measurement of materials, which is of primary importance for tribological surfaces. It is also very relevant to investigate plastic flow of pressure-dependent materials since it enforces shear flow and avoids isostatic compression contribution to the mechanical response of materials. It opens also the way to very high strain rate experiments, since shear can be applied on a very small gauge. With a better acquisition rate, it can be expected to reach higher orders of magnitude using this technique (i.e. 10 000 s^{-1}).

ACKNOWLEDGEMENTS

This work was supported by the RATES project (ANR-20-CE08-0022) and by the LABEX MANUTECH-SISE (ANR-10-LABX-0075) operated by French National Research Agency (ANR). The authors would also like to thank the Region Auvergne-Rhône-Alpes (within the SCUSI project) and "fédération IngéLyse" for their financial support.

CONFLICT OF INTEREST

The authors declare that they have no conflict of interest.

REFERENCES

1. W. C. Oliver and G. M. Pharr, Journal of Materials Research **7**, 1564 (1992).
2. J. Wehrs, G. Mohanty, G. Guillonneau, A. A. Taylor, X. Maeder, D. Frey, L. Philippe, S. Mischler, J. M. Wheeler, and J. Michler, JOM **67**, 1684 (2015).
3. A. Viat, G. Guillonneau, S. Fouvry, G. Kermouche, S. Sao Joao, J. Wehrs, J. Michler, and J.-F. Henne, Wear **392**, 60 (2017).
4. A. Dreano, S. Fouvry, S. Sao-Joao, J. Galipaud, and G. Guillonneau, Wear 203101 (2019).
5. G. Molnar, P. Ganster, A. Tanguy, E. Barthel, and G. Kermouche, Acta Mater. **111**, 129 (2016).
6. G. Molnar, G. Kermouche, and E. Barthel, Mech. Mater. **114**, 1 (2017).
7. C. Mayr, G. Eggeler, G. A. Webster, and G. Peter, Materials Science and Engineering: A **199**, 121 (1995).
8. J.-K. Heyer, S. Brinckmann, J. Pfetzing-Micklich, and G. Eggeler, Acta Materialia **62**, 225 (2014).
9. D. Rittel, S. Lee, and G. Ravichandran, Experimental Mechanics **42**, 58 (2002).
10. A. Dorogoy and D. Rittel, Experimental Mechanics **45**, 167 (2005).
11. A. Dorogoy and D. Rittel, Exp. Mech. **45**, 178 (2005).
12. A. Dorogoy and D. Rittel, Exp Mech **46**, 355 (2006).
13. A. Dorogoy and D. Rittel, Exp Mech **49**, 881 (2008).
14. A. Dorogoy, D. Rittel, and A. Godinger, Exp Mech **55**, 1627 (2015).

15. M. Ames, J. Markmann, and R. Birringer, Materials Science and Engineering: A **528**, 526 (2010).
16. M. Ames, M. Grewer, C. Braun, and R. Birringer, Materials Science and Engineering: A **546**, 248 (2012).
17. R. Rabe, J.-M. Breguet, P. Schwaller, S. Stauss, F.-J. Haug, J. Patscheider, and J. Michler, Thin Solid Films **469–470**, 206 (2004).
18. R. Lacroix, V. Chomienne, G. Kermouche, J. Teisseire, E. Barthel, and S. Queste, International Journal of Applied Glass Science **3**, 36 (2012).
19. G. Guillonneau, M. Mieszala, J. Wehrs, J. Schwiedrzik, S. Grop, D. Frey, L. Philippe, J.-M. Breguet, J. Michler, and J. M. Wheeler, Materials & Design (2018).
20. J. P. Best, G. Guillonneau, S. Grop, A. A. Taylor, D. Frey, Q. Longchamp, T. Schar, M. Morstein, J.-M. Breguet, and J. Michler, Surf. Coat. Technol. **333**, 178 (2018).
21. S. Breumier, S. Sao-Joao, A. Villani, M. Lévesque, and G. Kermouche, Materials & Design **193**, 108789 (2020).
22. G. Kermouche, G. Guillonneau, J. Michler, J. Teisseire, and E. Barthel, Acta Materialia **114**, 146 (2016).
23. G. Kermouche, E. Barthel, D. Vandembroucq, and Ph. Dubujet, Acta Materialia **56**, 3222 (2008).
24. R. Ramachandramoorthy, J. Schwiedrzik, L. Petho, C. Guerra-Nuñez, D. Frey, J.-M. Breguet, and J. Michler, Nano Lett. **19**, 2350 (2019).